Korean J. Chem. Eng., 32(5), 939-949 (2015)
DOI: 10.1007/s11814-014-0292-z

pISSN: 0256-1115
eISSN: 1975-7220

Monte Carlo simulation of free energy for the solid-liquid equilibrium of methane

Minkyu Kim and Jaeeon Chang†

Department of Chemical Engineering, University of Seoul, Siripdae-gil 13, Dongdaemun-gu, Seoul 130-743, Korea
(*Received 10 June 2014 • accepted 27 September 2014*)

Abstract−The thermodynamic properties of methane, particularly for solid-liquid equilibrium, are calculated by Monte Carlo simulation. For various potential models of methane, we explicitly calculated free energies and chemical potentials of the solid and liquid phases of methane by using the expanded ensemble method and the thermodynamic integration method. The Einstein-molecule method combined with the expanded ensemble method is used for the solid phase, and thermodynamic integration for the liquid phase. Coexistence properties such as melting temperature, entropy change and enthalpy change of melting are predicted and compared with experiment. Among the potential models studied, the OPLS-AA model shows the best performance in predicting the solid-liquid coexistence properties of methane. The melting temperature at zero pressure is predicted to be 92.6 K, in good agreement with the experimental value of 90.6 K. While other all-atom potential models reasonably predict the density of solid methane within an error of 5%, they tend to underestimate the melting temperature. The OPLS-AA potential model yields the most accurate value for the entropy change of melting, predicted to be 8.71 J/mol·K. This is within an error of 16%, compared to the experimental value of 10.4 J/mol·K. Also, the enthalpy change of melting is predicted to be 0.81 kJ/mol with an error of 14%, compared to the experimental value of 0.94 kJ/mol.

Keywords: Free Energy, Methane, Entropy, Monte Carlo, Melting Point

INTRODUCTION

Methane is an abundant chemical substance in the form of natural gas and gas hydrate. Its thermodynamic properties are important in developing novel technologies and instruments for mining, storage and transportation. At ambient pressure, solid methane exists as orientationally disordered crystal or plastic crystal (phase I) [1]. Upon increasing the pressure, the methane crystal transforms into orientationally ordered crystals such as phase III, IV, VI, A and B in which the rotational motions of molecules become (partially) suppressed [2-5]. The orientationally disordered crystal (phase I) has face-centered-cubic (FCC) structure. Phase I is located in the *PT* diagram adjacent to fluid phases, and the crystal of phase I at the atmospheric pressure is stable below the melting temperature of 90.6 K and above 20.4 K [1,6]. Below 20.4 K, the crystal transforms into orientationally partially ordered crystal of phase II in which the rotational motions of some molecules in unit cell become restricted.

To investigate the physical properties of methane crystals, many simulation studies have been done at the molecular level. Bounds et al. [7] carried out molecular dynamics (MD) simulation for methane crystal of the phase I with William's potential model [8]. They observed that crystal structure of the phase I predicted by MD simulation was in accord with the experiment. However, the values of energy and pressure obtained from the simulation were significantly different from the experimental values. In order to resolve such disagreement, they modified the Williams potential by adding damping factors [7]. With this modification, the predicted solid-solid phase transition between the phase I and II agreed with the experiment [9]. Recently, El-Sheikh et al. proposed a potential model of methane applicable to various crystal phases of methane over a wide range of pressure [10]. They simulated several crystal phases of methane and predicted solid-solid phase transitions by observing abrupt changes in energy. In addition, several specific potential models of methane have been developed to predict the thermophysical properties of solid and liquid phases [11-14]. To assess the accuracies of various potential models of methane, a simulation study was carried out for liquid methane at 150 K and the density of 28 mol/L [15]. It was found that the potential model of Murad et al. [16] and the OPLS-AA potential model [17] give good predictions for the properties of liquid methane. Yet, to our knowledge, a similar simulation study for the properties of solid methane and solid-liquid coexistence properties has not been attempted.

In this work, we evaluated the accuracies and performances of several selected potential models of methane for the thermodynamic properties, including the density of solid (phase I), melting temperature, entropy change and enthalpy change of melting. To predict the melting temperature, the free energy of methane crystal is calculated by the Einstein-molecule method combined with the expanded ensemble (EE) method [18,19], and the free energy of liquid methane is calculated by the thermodynamic integration (TI) method [20]. The EE method is also used to calculate the free energy of liquid so as to check the consistency of the free energy obtained from the TI method. This would be a rigorous test to validate the accuracy and reliability of the numerical schemes used in this work. From the comparison of simulation results for the solid-

†To whom correspondence should be addressed.
E-mail: changjaee@uos.ac.kr
‡This article is dedicated to Prof. Hwayong Kim on the occasion of his retirement from Seoul National Univerisity.

liquid coexistence properties at zero pressure, we chose the best potential model of methane. Then, using the Gibbs-Duhem integration method [21], we traced out a complete coexistence curve for the solid-liquid equilibrium of methane.

THEORY AND SIMULATION METHOD

1. Intermolecular Potential Model

To describe intermolecular interactions between methane molecules, we considered five potential models available in the literature: all-atom Lennard-Jones (LJ) potential models including the potential model of Murad et al. [16], the model of El-Sheikh et al. [10], the OPLS-AA model [17], the exponential-6 (Exp-6) model of Williams [8], and the TraPPE-UA model [22]. The pair interaction potential described by the LJ potential model is given as

$$u_{ij}(r)=4\varepsilon_{ij}\left[\left(\frac{\sigma_{ij}}{r}\right)^{12}-\left(\frac{\sigma_{ij}}{r}\right)^{6}\right]+\frac{q_i q_j}{4\pi\varepsilon_0 r}, \quad (1)$$

and the interaction potential described by the Exp-6 potential model is given as

$$u_{ij}(r)=A_{ij}\exp(-B_{ij}r)-\frac{C_{ij}}{r^6}, \quad (2)$$

where u_{ij} is the pair potential between two atoms i and j in different molecules, r is the distance, ε is the well depth, σ is the size parameter, q is the partial charge, and ε_0 is the permittivity of vacuum. The Exp-6 model consists of repulsion term characterized by A and B, and dispersion term of $-C/r^6$. The potential parameters, bond length and the moment of inertia of methane molecule in each potential model are summarized in Tables 1 and 2. The dispersion and electrostatic interactions are truncated at 11 Å based on the distance between the centers of mass of molecule, and standard long-range corrections for the dispersion interactions are added [20]. In Monte Carlo (MC) simulation, methane molecule is treated as a rigid body with tetrahedral geometry. The maximum magnitudes of translational and rotational moves of the molecules are chosen so as to yield the acceptance of 50%.

2. Expanded Ensemble Monte Carlo Simulation

Fig. 1 shows a schematic diagram for the Monte Carlo simulation of the solid-liquid phase equilibrium of methane. Simulation in each phase is performed independently, mimicking its own bulk phase with periodic boundary conditions applied to principal simulation box, and there is no actual phase boundary between the two simulation boxes. The chemical potentials of the individual phases are calculated in this work by the expanded ensemble Monte Carlo simulations and the thermodynamic integration method. Then,

Table 2. The CH bond length and the moment of inertia of molecule in the potential models of methane

Potential model	d_{CH} (Å)	I (10^{-47} kg m^2)
Murad et al.	1.10	5.401
El-Sheikh et al.	1.09	5.303
OPLS-AA	1.09	5.303
William	1.04	4.828
TraPPE-UA	0.0	0.0

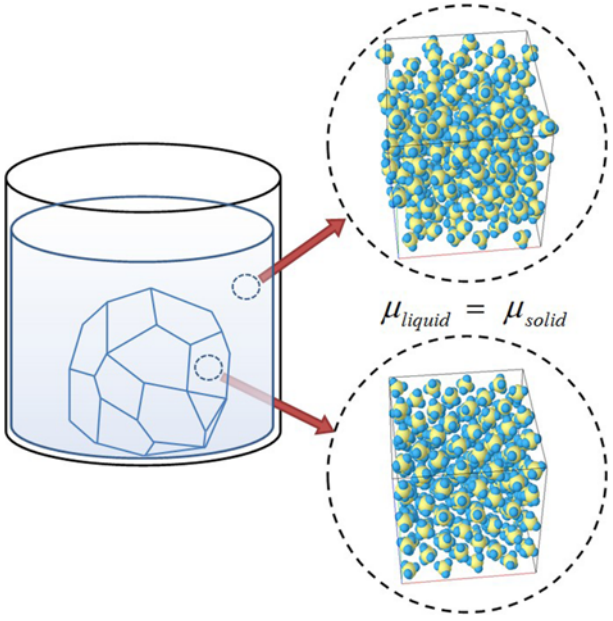

Fig. 1. Monte Carlo simulation of solid and liquid phases of methane. Periodic boundary conditions are applied to the simulation box of each phase to mimic bulk phase, and there is no physical phase boundary between the solid and liquid. Coexistence is found by the equality of chemical potential.

Table 1. The parameters of the potential models of methane. The well depth ε/k is in units of K, size parameter σ in Å and charge q in the electron charge, the Exp-6 potential parameter *A* in 10^7 K, B in Å^{-1} and C in 10^5 KÅ^6, respectively

LJ model	ε_{CC}/k	ε_{HH}/k	ε_{CH}/k	σ_{CC}	σ_{HH}	σ_{CH}	q_C	q_H
Murad et al. [16]	51.2	8.63	23.8	3.35	2.813	2.995	-	-
El-Sheikh et al. [10]	51.2	8.60	20.98	3.35	2.81	3.08	−0.572	0.143
OPLS-AA [17]	33.21	15.1	22.39	3.50	2.50	2.958	−0.24	0.06
TraPPE-UA [22]	148.0	-	-	3.73	-	-	-	-

Exp-6 model of William [8]	A_{CC}	B_{CC}	C_{CC}	A_{HH}	B_{HH}	C_{HH}
	3.115	3.60	2.541	0.1323	3.74	0.1625
	A_{CH}	B_{CH}	C_{CH}			
	0.5536	3.67	0.6441			

solid-liquid coexistence condition is found by the equality of chemical potentials. The approach taken in this work is free from cumbersome issues of hysteresis, and the absence of interface greatly reduces computational cost.

Prior to the free energy calculation, anisotropic *NPT* MC simulation of crystal is performed to determine its crystal structure and cell size [23,24]. Then, for the fixed crystal structure and volume, the Helmholtz free energy is calculated using the Einstein-molecule method [19,25]. In this method, a reference molecule is chosen and its position is fixed in space instead of constraining the center of mass of the system in the conventional Einstein-crystal methods [26,27]. The reference molecule, say, molecule 1, behaves like a free particle within the volume of system, and its contribution to the free energy is thus the same as that of an ideal-gas molecule. In simulation, the reference molecule carries lattice positions for the other molecules, each of which vibrates under its own external potential of which the center coincides with the fixed lattice position relative to that of the reference molecule.

The canonical partition function for a finite crystal consisting of N indistinguishable molecules as a spherical top is given by [19,25,28]

$$Q=\frac{V}{N\Lambda^{3N}}\frac{\pi^{N/2}}{\sigma_s^N\Omega^N}\left(\frac{8\pi^2 IkT}{h^2}\right)^{3N/2}\int\int e^{-U/kT}d\boldsymbol{\Omega}_1 d\mathbf{r}_2 d\boldsymbol{\Omega}_2\cdots d\mathbf{r}_N d\boldsymbol{\Omega}_N, \quad (3)$$

where Q is the canonical partition function, k is the Boltzmann constant, T is the temperature, V is the volume of system, Λ is the thermal wavelength given by $\Lambda=h/(2\pi mkT)^{1/2}$ with h being the Planck constant and m being the mass of molecule, U is the configurational energy, $\mathbf{r}_i$ is the position vector of molecule i, $\boldsymbol{\Omega}_i$ denotes the orientation of molecule i, $\Omega=8\pi^2$, σ_s is the symmetry number, and I is the moment of inertia of methane molecule. The configurational integral is divided by the number of molecules, N, which is regarded as the number of physically feasible permutations of the crystal as a whole realized by translation while mimicking bulk crystal of infinite size by using periodic boundary conditions. In the free energy simulation, the reference molecule (molecule 1) is fixed in space while separately accounting for its translational contribution to the partition function as V/Λ. An advantage of the Einstein-molecule method is that the crystal is prevented from drifting because of the presence of the spatially fixed reference molecule even when the external potential is turned off as in the real crystal. The external potential for a molecule in the Einstein crystal is described by

$$u^{Ein}(\mathbf{r})=\lambda_t(\mathbf{r}-\mathbf{r}_0)^2+\lambda_\theta(1-\cos\theta)+\lambda_\omega(1-\cos\omega), \quad (4)$$

where λ_t is translational force constant, λ_θ and λ_ω are rotational force constants, $\mathbf{r}$ is the position vector of the center of mass of molecule, $\mathbf{r}_0$ is its equilibrium position, (ϕ, θ, ψ) are the Euler angles, and ω is given by $\omega=\phi+\psi$ [29,30]. The first term in the right-hand side of Eq. (4) is the translational part of the external potential applied to all molecules except for the reference molecule. The last two terms are orientational parts that constrain the orientation of the molecule. The orientational external potential is needed for ordered and partially ordered crystals, but they are not necessarily required for disordered crystals, for instance, the methane crystal of phase I and the high-temperature fullerene crystals [25,31]. The translational part of the free energy of the Einstein crystal with a fixed reference molecule is given by [19,28]

$$\frac{\beta A_t^{Ein}}{N}=\frac{1}{N}\ln\left(\frac{N}{V}\right)-\frac{3}{2}\left(1-\frac{1}{N}\right)\ln\left(\frac{\pi}{\beta\lambda_t}\right)+3\ln\Lambda, \quad (5)$$

where A is the Helmholtz energy and β is 1/kT. The force constants of the external potential are chosen so that each of positional and orientational distribution of the molecules in the Einstein crystal closely resembles the corresponding distribution in the real crystal. In this way, the translational force constant λ_t is set to 13 kJ/mol·Å^2 for the methane crystal of phase I.

The orientational part of free energy of the Einstein crystal is given by [25,30,31]

$$\frac{\beta A_o^{Ein}}{N}=\ln\frac{2\beta\lambda_\theta}{1-\exp(-2\beta\lambda_\theta)}+\beta\lambda_\omega-\ln[I_0(\beta\lambda_\omega)]-\ln\frac{\sqrt{\pi}}{\sigma_s}\left(\frac{8\pi^2 I}{\beta h^2}\right)^{\frac{3}{2}}, \quad (6)$$

where I_0 is the Bessel function. For the orientationally disordered crystal phase considered here, there is no need of imposing rotational external potentials, whereas sensibly chosen values for the rotational force constants are needed for (partially) ordered phases [25,31]. Thus, in the present case of solid methane (phase I), we simply set $\lambda_\theta=\lambda_\omega=0$, and the orientational free energy of the Einstein crystal is the same as that of an ideal gas. This does not mean, however, that the orientational distribution of the molecules in real crystal is perfectly uniform, but rather implies that probability for the orientational distribution is non-zero at any orientations.

As the methane molecule is treated as a rigid body, vibrational contributions to the entropy and the Helmholtz energy are ignored. In reality, the amplitude of CH bond vibration is less than only a few percent of the bond length, and HCH angle bending occurs only within a few degrees. The rigid structure of methane molecule frozen at the equilibrium configuration does not significantly change the configurational properties such as energy and pressure. Quantum mechanical contribution of each normal mode of vibration to the entropy and free energies can be included for completeness [32]. However, this would not affect the determination of phase equilibrium since the vibrational contributions depend only on the temperature, independent of the volume of the system, and their contributions to the chemical potentials are cancelled between solid and liquid phases coexisting at the same temperature.

The symmetry number σ_s is set to twelve for the crystal of phase I, the same as that of fluid phase. The symmetry number makes a quantum mechanical correction to the Maxwell-Boltzmann statistics so as not to overcount indistinguishable orientational configurations. As usual, the symmetry number in gas or liquid phase is considered as an intrinsic property of a molecule that is independent of thermodynamic state. However, in crystals, the symmetry number depends also on the rotational characteristics of the molecules confined within their lattice cells [25,31]. At sufficiently low temperatures the rotational motions of the molecules in crystals are restricted by high energy barriers compared with kT. The crystal becomes orientationally ordered phase in which the time trajectory of the system samples only a fragment in phase space out of many possible orientational configurations. For example, in the orientationally ordered phase (phase III) of methane, a molecule can access only one orientational configuration out of the twelve possible orientational configurations. Therefore, a proper value of

the symmetry number for the phase III is unity. However, in the orientationally disordered phase (phase I), a molecule can access all the twelve orientational configurations with almost free rotation. Therefore, the proper value of the symmetry number for the phase I is twelve, the same as those of gas and liquid phases. We also note that, unlike the present approach, there is another free energy approach that uses symmetric orientational field reflecting the symmetry of molecule together with adopting the symmetry number of ideal-gas molecule [33,34]. Despite the seemingly contradictory views of the symmetry number, either approach should lead to the same result for entropy and its derived properties.

In the expanded ensemble MC simulation (EEMC) of solid phase [25,31,35-37], the energy of the system varies linearly with a coupling parameter ranging from zero for the reference Einstein crystal to unity for the real crystal,

$$U(\lambda)=\lambda\sum_{i<j}u_{ij}+(1-\lambda)\sum_{i}u_{i}^{Ein}, \tag{7}$$

In the EEMC simulation of fluid phase, the two-stage WCA scaling is used for the LJ potential models [38-43]. In the first stage of coupling interactions between a solute molecule and N solvent molecules ($0\le\lambda\le1$), repulsive LJ interaction is turned on by varying the size parameter as

$$u_{LJ}^{rep}(r;\lambda)=\begin{cases}4\varepsilon\left[\left(\frac{\sigma_\lambda}{r}\right)^{12}-\left(\frac{\sigma_\lambda}{r}\right)^{6}\right]+\varepsilon, & r<2^{1/6}\sigma_\lambda,\\ 0, & r\ge2^{1/6}\sigma_\lambda,\end{cases} \tag{8}$$

The LJ potential is truncated at the distance at which the potential has a minimum, and it is shifted upwards by the well depth ε. The size parameter σ_λ is scaled by $\sigma_\lambda=\lambda^{1/3}\sigma$ because the free energy is roughly proportional to the volume of repulsive core. When the size parameter is fully grown in the first stage, it is subsequently followed by the second stage ($1\le\lambda\le2$) in which attraction and electrostatic interactions are turned on linearly as

$$u_{LJ}^{att}(r;\zeta)=\begin{cases}-\zeta\varepsilon, & r<2^{1/6}\sigma,\\ 4\zeta\varepsilon\left[\left(\frac{\sigma}{r}\right)^{12}-\left(\frac{\sigma}{r}\right)^{6}\right], & r\ge2^{1/6}\sigma,\end{cases} \tag{9}$$

$$u_{el}(r;\zeta)=\zeta\frac{q_iq_j}{4\pi\varepsilon_0 r}, \tag{10}$$

where ζ ($=\lambda-1$) is a linear scaling parameter for the second stage ($0\le\zeta\le1$).

The partition function of the expanded ensemble is a weighted sum of the partition functions of subensembles given by

$$Q_E(N,V,T)=\sum_{i}\exp(w_i)Q(N,V,T;\lambda_i), \tag{11}$$

where w_i is weight factor for the i-th subensemble associated with the coupling parameter λ_i. Transitions between adjacent subensembles ($\lambda_i\leftrightarrow\lambda_j$) are accepted by the Metropolis criterion with the weight factors [18]. Free energy difference between two subsystems is derived from Eq. (11) as

$$\beta A_j-\beta A_i=w_j-w_i-\ln(P_j/P_i), \tag{12}$$

where P_i is the probability for the system of being in the i-th subensemble during EEMC simulation. For the EEMC simulation of solid, the free energy difference between the Einstein crystal and real crystal is given by

$$\beta\Delta A=w_M-w_0-\ln(P_M/P_0), \tag{13}$$

where the subscripts 0 and M denote the first subensemble (Einstein crystal) and the last subensemble (real crystal), respectively. The other M−1 intermediate subensembles observed in the EEMC simulation, though they are not physical, provide a smooth path between the two ends. Similarly, excess chemical potential of liquid is given by

$$\beta\mu^{ex}=w_M-w_0-\ln(P_M/P_0), \tag{14}$$

where μ^{ex} is the chemical potential of solute in excess of that of ideal gas at the same temperature and density of solvent, and the subscripts 0 and M denote the system containing N molecules (pure solvent) and that containing N+1 molecules (solution with an added solute molecule), respectively. The details of implementing EEMC simulation for the solid and liquid phases and how to optimize the weight factors on the fly are referred to our previous studies [35, 42,43]. Adding up the individual contributions, the free energy of the solid and the chemical potential of the liquid are written as

$$A_{solid}=A_o^{Ein}+A_t^{Ein}+\Delta A, \tag{15}$$

$$\mu_{liquid}=\mu_{ideal}+\mu^{ex}, \tag{16}$$

For the chemical potential, a standard long range correction is added, given by $\mu_{LRC}=2U_{LRC}/N$, i.e., twice the long range correction for the configurational energy per molecule [20].

3. Thermodynamic Integration and Gibbs-Duhem Integration Methods

The free energy of a liquid is calculated by thermodynamic integration [20] on a reversible path starting from an ideal gas to a liquid of desired density and temperature while bypassing vapor-liquid phase transition,

$$\frac{A(\rho_2,T)}{N}=\frac{A(\rho_1,T)}{N}+\int_{\rho_1}^{\rho_2}\frac{P(\rho)}{\rho^2}d\rho \text{ (at constant T)}, \tag{17}$$

$$\frac{A(\rho,T_2)}{NT_2}=\frac{A(\rho,T_1)}{NT_1}-\int_{T_1}^{T_2}\frac{E(T)}{NT^2}dT \text{ (at constant } \rho), \tag{18}$$

where ρ (=N/V) is the number density, P is the pressure, and E is the internal energy. The thermodynamic integration is comprised of two steps. In the first step, *NPT* MC simulations are performed at a constant temperature above the critical temperature and at a series of pressures gradually varying from that of the ideal gas to that of the liquid of a desired density. Volumetric data gathered from the simulations are used to integrate Eq. (17), which gives free energy difference between the ideal gas and the liquid at the same temperature. In the second step, *NVT* MC simulations are performed at the constant liquid density and at a series of temperatures gradually varying from the supercritical temperature to a desired temperature of the liquid of interest. The internal energies obtained from the simulations, as the sum of average configurational energy and kinetic energy, are used to integrate Eq. (18), which gives free energy difference over the range of temperature. Thus, the absolute value of free energy of the liquid of interest is obtained as a

sum of the free energy of the ideal gas and the free energy differences obtained from the two thermodynamic integration steps. Note that the average kinetic energy, 3RT, is used for the all-atom models, while the term (3/2)RT is used for the united-atom model of TraPPE-UA potential. The details of calculating the free energy of liquid methane with the thermodynamic integration method are further discussed in the next section.

Once the coexistence condition is determined at a fixed pressure, a complete solid-liquid coexistence curve can be predicted by the Gibbs-Duhem integration method [21]. This is in fact the same as integrating the Clapeyron equation given by

$$\frac{dP}{dT} = \frac{\Delta H}{T\Delta V}, \tag{19}$$

where ΔH and ΔV are differences in enthalpy and volume between coexisting solid and liquid phases, respectively. Starting from the melting temperature of methane determined at zero pressure, we integrate Eq. (19) in discretized form with performing *NPT* MC simulations of the two phases to obtain the enthalpy and volume differences.

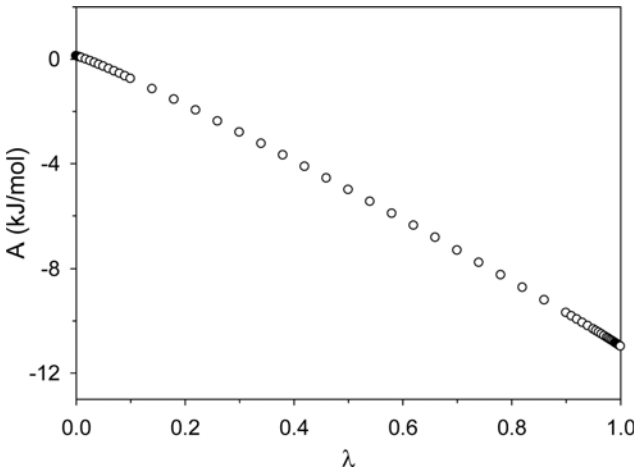

Fig. 2. The Helmholtz energy of solid methane at 60 K and zero pressure obtained from the EEMC simulation for the OPLS-AA potential model. The coupling parameter λ is varied from zero for the reference Einstein crystal to unity for the real crystal.

RESULTS AND DISCUSSION

For the five potential models of methane, anisotropic *NPT* MC simulations were performed to obtain the density of solid methane (phase I). Table 3 presents simulation results of the density of methane crystal at zero pressure below the experimental melting temperature, 90.6 K. The observed crystal structures of solid methane in the simulations are indeed FCC structures. The values of the density predicted for the potential models of Murad et al. and El-sheikh et al. agree with experimental densities [44] within an error of 5%. While the two potential models differ from each other in the presence of charges, the effects of charge on the density are less significant due to the cancellation of dipole moments along CH bonds. For the OPLS-AA model, the predicted densities of the solid are higher than the experimental values with an error of about 13%. This discrepancy is probably because the well depth of hydrogen atom in the OPLS-AA model, optimized for a series of alkane liquids near the room temperature [17], might be too strong for low-temperature methane crystal. The strong attraction would increase the density of the crystal, and it would also render the crystal more stable. Similar overestimations for the density of methane crystal are observed with the Williams model and the TraPPE-UA model.

The Helmholtz energies of the methane crystal are calculated by the EEMC simulation together with the Einstein-molecule method. The simulations are conducted for the crystals of FCC structure at the fixed density that was determined from the previous *NPT* MC simulations. In Fig. 2, for the OPLS-AA potential model the Helmholtz energy of the crystal at 60 K and zero pressure is plotted versus the coupling parameter λ. To obtain high precision results, a step size of 0.04 in λ is chosen. For λ>0.9 and λ<0.05, smaller step sizes were needed to maintain the same order of precision and also to obtain flat distribution along the λ coordinate in the EEMC simulation. For λ<0.05, when intermolecular interactions between the molecules begin to turn on, repulsive interaction energies change drastically. For λ>0.9, when the Einstein field is being turned off, configurational overlaps between adjacent subensembles become quite reduced. In these circumstances, even smaller step sizes are used as shown in Fig. 2. In Table 4, we present simulation results for the configurational energies of the solid and liquid methane at zero pressure with varying the temperature. In Table 5 are the simulation results for the Helmholtz energy of the solid methane calculated by the EEMC method combined with the Einstein-molecule method. In the EEMC simulation, each run was carried out for 3.0×10^6 cycles, while a shorter run of 3.0×10^5 cycles in *NPT* MC simulation was sufficient to obtain accurate values of the configurational energy. As seen in Table 4, the configurational energy tends to increase with the increasing temperature, and the configurational energy of the liquid methane is higher than that of the solid due to enhanced thermal motion. In contrast, the Helmholtz energy de-

Table 3. *NPT* MC simulation results for the density of methane crystal (phase I) at zero pressure. The numbers in parentheses are simulation uncertainties in last digit

T (K)	Density (g/cm^3)					
	Expt. [44]	Murad et al.	El-Sheikh et al.	OPLS-AA	William	TraPPE-UA
60	0.500	0.49047(2)	0.48761(3)	0.56610(10)	0.52659(5)	0.53260(4)
65	0.497	0.48460(10)	0.48220(10)	0.56121(1)	0.52190(10)	0.52882(5)
70	0.494	0.47900(7)	0.47684(2)	0.55640(8)	0.51737(1)	0.52484(5)

Table 4. *NPT* MC simulation results for the configurational energy of the solid and liquid methane at zero pressure

T (K)	Phase	Configurational energy (kJ/mol)				
		Murad et al.	El-Sheikh et al.	OPLS-AA	William	TraPPE-UA
60	Solid	−9.446(2)	−9.398(1)	−10.837(3)	−9.324(1)	−9.8003(1)
65	Solid	−9.281(1)	−9.242(2)	−10.695(1)	−9.203(2)	−9.7093(1)
70	Solid	−9.120(1)	−9.087(1)	−10.557(1)	−9.084(1)	−9.6152(1)
75	Solid	-	−8.930(3)	−10.416(2)	−8.958(2)	−9.5180(1)
95	Liquid	−7.640(2)	−7.479(2)	−9.006(4)	−7.645(1)	-
100	Liquid	−7.434(1)	−7.2694(3)	−8.801(6)	−7.464(1)	-
105	Liquid	−7.220(4)	−7.0626(3)	−8.593(2)	−7.279(2)	−7.470(1)
110	Liquid	−7.007(5)	−6.8460(5)	−8.392(3)	−7.100(4)	−7.305(4)

Table 5. The Helmholtz energy of methane crystal (phase I) at zero pressure obtained from the EEMC simulation

T (K)	Helmholtz energy (kJ/mol)				
	Murad et al.	El-Sheikh et al.	OPLS-AA	William	TraPPE-UA
60	−9.814(1)	−9.762(1)	−10.981(1)	−9.891(1)	−9.941(1)
65	−9.981(1)	−9.929(1)	−11.127(2)	−10.073(2)	−10.022(1)
70	−10.165(1)	−10.115(1)	−11.293(1)	−10.274(2)	−10.112(1)
75	-	−10.314(1)	−11.481(1)	−10.489(1)	−10.215(1)

creases as the temperature increases, as seen in Table 5. Clearly, the decrease of the free energy results from the positive entropy that increases with the temperature.

The Helmholtz energies of liquid methane are calculated by the thermodynamic integration method as well as the EEMC method. The values of the free energy obtained from both methods are compared so as to check the consistency and accuracy of the two free energy calculations. The EEMC simulations of the liquid are conducted at the fixed density that was determined from the previous *NPT* MC simulations at zero pressure. In Fig. 3, for the OPLS-AA potential model we show the values of the excess chemical potential of liquid methane at 110 K and zero pressure along the coupling parameter λ. Note that the chemical potential at zero pressure is the same as the molar Helmholtz energy. As explained in the preceding section, the EEMC simulation is done in two stages; the repulsion part is turned on for $0 \le \lambda \le 1$, and the attraction and electrostatic parts are subsequently turned on for $1 \le \lambda \le 2$.

In Fig. 4, for the OPLS-AA potential we show the Helmholtz energy of liquid methane at 110 K and zero pressure calculated by

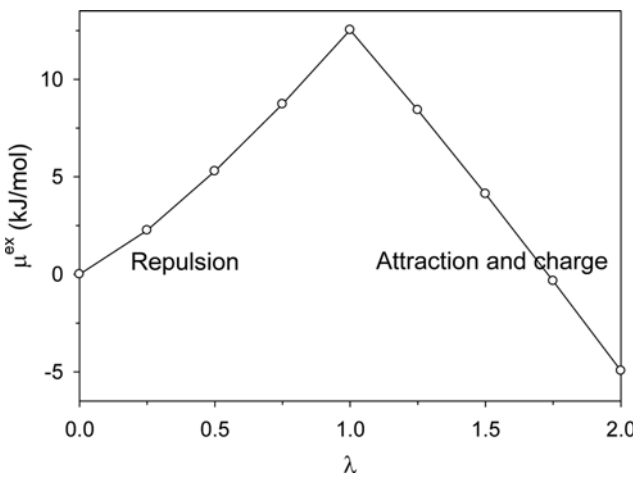

Fig. 3. The excess chemical potential of liquid methane at 110 K and zero pressure obtained from the EEMC simulation for the OPLS-AA potential model. The coupling parameter λ is varied in two stages: $0 \le \lambda \le 1$ for the repulsion and $1 \le \lambda \le 2$ for the attraction and charge.

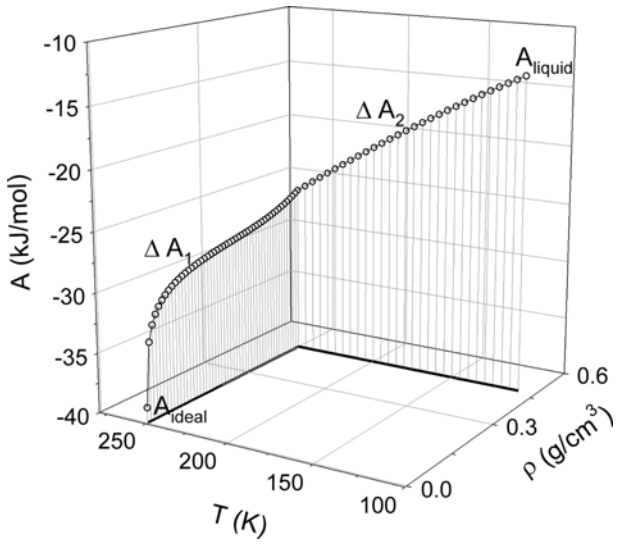

Fig. 4. The Helmholtz energy of liquid methane obtained from the thermodynamic integration. The integration paths are shown as the thick lines at the bottom. A_{ideal} is the Helmholtz energy of the ideal gas of methane at 250 K and 1 bar, and A_{liquid} is the Helmholtz energy of liquid methane at 110 K and zero pressure with the density of 0.47234 g/cm^3. ΔA_1 and ΔA_2 are the free energy differences obtained for the constant temperature path and for the constant density path, respectively.

the TI method. An ideal gas of methane at 250 K and 1 bar is used as a reference system with known free energy. Simulations with the TI method are conducted in two steps following the integration paths drawn in Fig. 4 as the thick lines. In the first step, *NPT* MC simulations are conducted at 250 K, well above the critical temperature of 190.4 K, with varying the pressure so that the ideal gas is reversibly compressed to a fluid of the desired density, 0.47234 g/cm^3, which was determined from *NPT* MC simulation at 110 K and zero pressure. Simulation results for the volumetric data of pressure vs. density are collected, and the pressure is fitted with a suitable polynomial in density. Then, the thermodynamic integration of Eq. (17) is analytically evaluated on the isotherm. Free energy difference obtained in this constant-temperature step is depicted as ΔA_1 in Fig. 4. By avoiding spurious vapor-liquid phase transition, the free energy changes smoothly along the path. Next, *NVT* MC simulations at the fixed liquid density are conducted with varying the temperature from 250 K to 110 K, which completes the thermodynamic path to the target liquid at 110 K and zero pressure. In these simulations, the average values of the configurational energy varying with the temperature are collected. Fitting the internal energy with a suitable polynomial in temperature, the thermodynamic integration of Eq. (18) is evaluated analytically along the isochore. Free energy difference for the constant-density step is denoted as ΔA_2 in Fig. 4. The absolute value of the free energy of liquid methane at 110 K and zero pressure is obtained as a sum of the free energy of the ideal gas and the free energy differences, ΔA_1 and ΔA_2, along the path of thermodynamic integration,

$$A_{liquid}=A_{ideal}+\Delta A_1+\Delta A_2, \tag{20}$$

In Table 6 we compare the values of the Helmholtz energy of liquid methane at zero pressure obtained from the EE and TI methods. Each run of the EEMC simulation is sampled for 3.0×10^6 cycles, and each run of *NPT* MC simulation for the TI method is sampled for 2.0×10^5 cycles. As depicted in Fig. 4, the absolute value of the free energy of liquid methane at 110 K is first obtained from the TI method. Relative to this value, free energies at other temperatures are calculated by the thermodynamic integration of the Gibbs-Helmholtz (GH) equation given by

$$\left[\frac{\partial(G/T)}{\partial T}\right]_P=-\frac{H}{T^2}, \tag{21}$$

Here, the enthalpy and Gibbs energy at zero pressure are the same as the internal energy and the Helmholtz energy, respectively. Of course, the GH integration of Eq. (21) is a kind of TI method along the isobar.

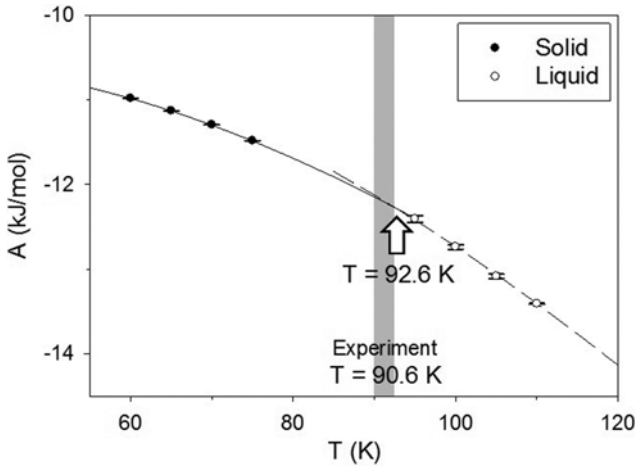

Fig. 5. The Helmholtz energies of solid and liquid methane at zero pressure for the OPLS-AA potential model. The symbols are obtained from the EEMC simulations, and the curves are from the thermodynamic integration of the Gibbs-Helmholtz equation. The melting temperature is predicted to be 92.6 K, close to the experimental value of 90.6 K.

As seen in Table 6, the values of the Helmholtz energy of liquid methane obtained from the EE and TI methods are in excellent agreement with each other, whereas the two methods are based on seemingly different theoretical foundations. In computational aspects, in order to achieve similar accuracies for the free energy of liquid, the EEMC simulation requires much longer computer time than the TI method together with the GH integration. Provided that the free energy at one temperature is at hand, predicting the free energy at other temperatures through the GH integration only requires the internal energy (or enthalpy), which is readily available from the conventional simulations with high accuracy. In favor of such computational advantage of the TI method (together with the GH integration) particularly for liquid, we adopt the TI method as a primary tool of calculating the free energy of liquid methane, and use the EEMC method to check the consistency of the results obtained from the TI method.

In Fig. 5, using the OPLS-AA potential model the melting temperature of methane at zero pressure is determined from the free energy profiles of the solid and liquid. Here, note that the molar Helmholtz energy at zero pressure is the same as the chemical potential. To obtain the free energy profiles, we carry out the GH inte-

Table 6. The Helmholtz energy of liquid methane at zero pressure obtained from the EEMC simulation and the thermodynamic integration (TI) method

T (K)	Helmholtz energy (kJ/mol)					
	Murad et al.		El-Sheikh et al.		OPLS-AA	
	EE	TI	EE	TI	EE	TI
95	−11.59(4)	−11.59	−11.47(5)	−11.48	−12.41(4)	−12.42
100	−11.90(2)	−11.93	−11.83(4)	−11.82	−12.74(3)	−12.73
105	−12.29(2)	−12.29	−12.21(4)	−12.18	−13.08(2)	−13.06
110	−12.65(2)	−12.66	−12.58(5)	−12.56	−13.41(1)	−13.41

Table 7. The melting temperature of methane, the entropy change and enthalpy change of melting

	Expt. [6]	Murad et al.	El-Sheikh et al.	OPLS-AA	William	TraPPE-UA
T_m (K)	90.6	69.9	79.5	92.6	83.0	105.3
ΔS (J/mol·K)	10.4	5.81	8.57	8.71	7.95	13.1
ΔH (kJ/mol)	0.94	0.41	0.68	0.81	0.66	1.38

gration of Eq. (21) for each phase. As starting points of the GH integrations, the free energy of solid methane at 60 K determined from the EEMC simulation and the free energy of liquid methane at 110 K determined from the TI method are used, respectively. In Fig. 5 the free energies from the GH integrations are drawn as the curves, and those from independent EEMC simulations are plotted as the symbols. The results from both methods are in excellent agreement with each other, and the consistency between the two methods is confirmed. The intersection of the free energy curves of the solid and liquid phases gives the melting temperature, which is found to be 92.6 K for the OPLS-AA model. This value agrees with the experimental melting temperature of 90.6 K at ambient pressure [6].

In the same manner, we predict melting temperatures for other potential models of methane, and they are compared in Table 7. Among the potential models we studied, the melting temperature of the OPLS-AA potential model, 92.6 K, is the closest to the experimental value. The melting temperatures for the Murad et al. model, the El-sheikh et al. model and the Williams model are predicted to be 69.9 K, 79.5 K and 83.0 K, respectively, and they are lower than the experimental value of 90.6 K. The melting temperature of the TraPPE-UA model was found to be 105.3 K, which is somewhat higher than the experiment. While the El-sheikh et al. model has strong charges to describe crystal phases at high pressures, its dispersion attraction seems not strong enough to sustain stable solid phase. This would be the reason why the melting temperature is underestimated by the El-sheikh et al. model as well as the Murad et al. model that is the prototype of the former.

In Fig. 6, for the OPLS-AA potential model we show the entropies of the solid and liquid methane. The entropy is obtained from the difference between the internal energy and the Helmholtz energy, i.e., $S=(U_c+3RT-A)/T$. Here, 3RT is the kinetic part of the internal energy for all-atom models, while the term of (3/2)RT is used for the TraPPE-UA model. The symbols are obtained from the EEMC

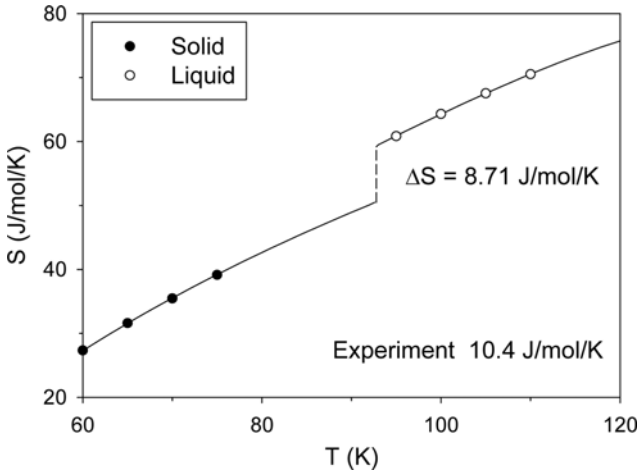

Fig. 6. The entropies of solid and liquid methane at zero pressure varying with the temperature for the OPLS-AA potential model. The symbols are obtained from the EEMC simulations, and the curves are from the thermodynamic integration of the Gibbs-Helmholtz equation. The entropy change at the melting transition is found to be 8.71 J/mol·K, compared to the experimental value of 10.4 J/mol·K.

simulations as given in Tables 5 and 6, and the curves are obtained from the GH integration in the similar manner as in Fig. 5. As shown in Fig. 6, the two sets of values for the entropy obtained from the two methods almost coincide with each other. The entropy of the solid phase from the GH integration reveals a slightly nonlinear behavior near the melting transition. The entropy change of melting is found by extending the curves to the calculated melting temperature. For the OPLS-AA model, ΔS is found to be 8.71 J/mol·K, slightly less than the experimental value of 10.4 J/mol·K [6] with an error of 16%. In the same manner, entropies for other potential models are calculated, and they are compared in Table 8. Because

Table 8. The entropies of solid and liquid methane. The entropy is obtained from the difference between the Helmholtz energy and the internal energy

T (K)	Entropy (J/mol·K)					
	Phase	Murad et al.	El-Sheikh et al.	OPLS-AA	William	TraPPE-UA
60	Solid	31.10	30.99	27.33	34.40	14.83
65	Solid	35.71	35.49	31.59	38.34	17.29
70	Solid	39.88	39.62	35.45	41.96	19.56
75	Solid	-	43.38	39.15	45.32	21.76
95	Liquid	66.56	67.03	60.82	66.92	-
100	Liquid	69.92	70.47	64.29	70.07	-
105	Liquid	73.26	73.70	67.52	73.05	46.55
110	Liquid	76.39	76.94	70.51	75.92	48.70

of the absence of the rotational part in the united atom model, the entropy of the TraPPE-UA model is significantly less than that of the all-atom models. The entropy changes of melting for other potential models are obtained in a similar manner as in Fig. 6, and are compared in the second row of Table 7. Among them, ΔS for the OPLS-AA potential model, 8.71 J/mol·K, is the most accurate when compared with the experimental value of 10.4 J/mol·K. The potential model of Murad et al. gives the least value of 5.81 J/mol·K, and the TraPPE-UA model gives the largest value of 13.1 J/mol·K. As we have the entropy change of melting, the enthalpy change of melting is readily obtained by $\Delta H=T_m\Delta S$. The comparison of ΔH is given in the last row of Table 7. Compared with the experimental value of 0.94 kJ/mol, ΔH for the OPLS-AA model yields the most accurate value of 0.81 kJ/mol with an error of 14%. Despite the fact that the OPLS-AA potential model has not been tuned for the thermodynamic properties of methane crystal, such a good agreement is remarkable.

Finally, using the Gibbs-Duhem integration method we predict the complete solid-liquid coexistence curve of methane with the OPLS-AA potential model. The predicted melting temperature of 92.6 K at zero pressure is used as a starting point for the integration of the Clapeyron equation, Eq. (19). To sample enthalpies and volumes of the individual phases, *NPT* MC simulations were run for 1.0×10^5 cycles at each integration step. In Fig. 7, we compare the predictions of the solid-liquid coexistence of methane with the experiment. The open circles are the simulation results, and the closed circles are the experimental coexistence data [45-47]. The upper left region is the solid phase of methane (phase I), and the lower right region is the liquid phase. The coexistence curve predicted by the simulation is slightly shifted to the right, indicating that the calculated melting temperature at a given pressure is a little higher than the experimental value. Considering the wide ranges of temperature and pressure, the predicted solid-liquid coexistence of methane with the OPLS-AA model is quite satisfactory. The present study shows that among the various potential models tested in this work, the OPLS-AA model provides, up to the present, the most accurate description of the solid-liquid phase equilibrium of methane.

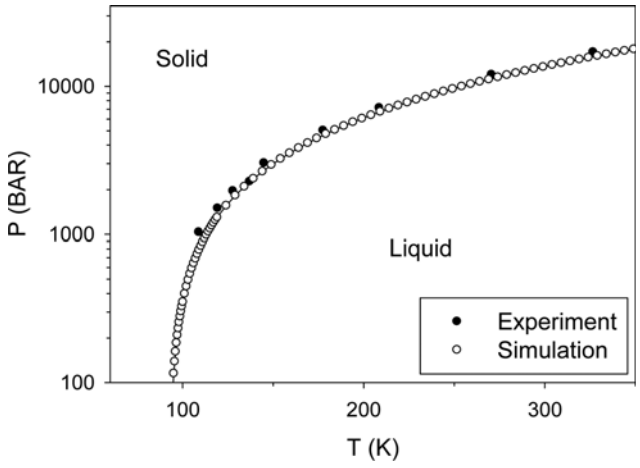

Fig. 7. The solid-liquid coexistence of methane obtained from the Gibbs-Duhem integration method for the OPLS-AA potential model. The closed circles are the experimental data, and the open circles are the simulation results.

CONCLUSIONS

Using various potential models of methane, we carried out MC simulations to predict the thermodynamic properties of solid and liquid methane, such as the density of plastic crystal (phase I), the free energies and entropies of the solid and liquid phases. Calculating the free energies with the EE and TI methods, we predicted melting temperature, entropy change and enthalpy change of melting. Among the five potential models examined, the OPLS-AA model gives the most accurate predictions for the solid-liquid coexistence properties. The melting temperature of methane at zero pressure is predicted to be 92.6 K, in good agreement with the experimental value of 90.6 K. Further, using the Gibbs-Duhem integration method and the OPLS-AA model, we accurately predicted a complete solid-liquid coexistence curve over the wide range of temperature and pressure.

There are, however, some shortcomings in the potential models of methane. The density of solid methane predicted by the OPLS-AA model is somewhat higher than the experimental value by about 10%, the entropy change of melting is underestimated by 16%, and the enthalpy change of melting is underestimated by 14%. The other all-atom potential models such as the Murad et al. model, the El-Sheikh et al. model and the Williams model reasonably predict the density of solid methane within an error of 5%, but the melting temperature and the entropy change of melting are poorly predicted. For the TraPPE-UA model, the predicted melting temperature is higher than the experiment. The entropy of the TraPPE-UA model is considerably lower than those of the all-atom potential models due to the absence of the rotational part, and the entropy change of melting was not accurately predicted. Judging from the present simulation results, we conclude that although the OPLS-AA potential model predicts the density of methane crystal (phase I) somewhat higher than the experiment, it is one of the most successful potential models for methane that can describe the solid-liquid equilibrium and the coexistence properties.

ACKNOWLEDGEMENT

This work was supported by the University of Seoul 2014 Research Fund.

NOMENCLATURE

A : Helmholtz energy
A_{ij} : potential parameter of Exp-6 potential
B_{ij} : potential parameter of Exp-6 potential
C_{ij} : potential parameter of Exp-6 potential
d : bond length
E : internal energy
G : Gibbs energy
H : enthalpy
h : Planck constant
I : moment of inertia

I_0 : Bessel function
k : Boltzmann constant
m : mass of molecule
N : number of molecules
P : pressure
P_i : probability of observing the i-th system
Q : partition function
q : partial charge
R : gas constant
r : distance
r : position vector of molecule
$\mathbf{r}_0$: equilibrium position vector of molecule
S : entropy
T : temperature
U : potential energy
U_C : configurational energy
u : interatomic potential energy
V : volume
w : weight factor

Greek Letters

β : inverse of kT
ε : Lennard-Jones energy parameter
ε_0 : permittivity of vacuum
θ : Euler angle
Λ : thermal de Broglie wavelength
λ : coupling parameter
λ_α : force constant
μ : chemical potential
ρ : density
σ : Lennard-Jones size parameter
σ_s : symmetry number
ϕ : Euler angle
ψ : Euler angle
Ω : orientation of molecule
ω : Euler angle

Superscripts

att : attraction
Ein : Einstein crystal
el : electrostatic interaction
ex : excess
rep : repulsion

Subscripts

C : carbon atom
E : expanded ensemble
H : hydrogen atom
ideal : ideal gas
liquid : liquid
LRC : long range correction
M : last subensemble
m : melting
o : orientation
solid : solid
t : translation

REFERENCES

1. W. Press, *J. Chem. Phys.*, **56**, 2597 (1972).
2. M. M. Thiéry, D. Fabre and K. Kobashi, *J. Chem. Phys.*, **83**, 6165 (1985).
3. P. Hebert, A. Polian, P. Loubeyre and R. Le Toullec, *Phys. Rev. B*, **36**, 9196 (1987).
4. R. Bini, L. Ulivi, H. J. Jodl and P. R. Salvi, *J. Chem. Phys.*, **103**, 1353 (1995).
5. R. Bini and G. Pratesi, *Phys. Rev. B*, **55**, 14800 (1997).
6. NIST Chemistry WebBook, http://webbook.nist.gov/chemistry.
7. D. G. Bounds, M. L. Klein and G. N. Patey, *J. Chem. Phys.*, **72**, 5348 (1980).
8. D. E. Williams, *J. Chem. Phys.*, **47**, 4680 (1967).
9. R. Righini, K. Maki and M. L. Klein, *Chem. Phys. Lett.*, **80**, 301 (1981).
10. S. M. El-Sheikh, K. Barakat and N. M. Salem, *J. Chem. Phys.*, **124**, 124517 (2006).
11. S. Fitzwater and L. S. Bartell, *J. Am. Chem. Soc.*, **98**, 5107 (1976).
12. M. Schoen, C. Hoheisel and O. Beyer, *Mol. Phys.*, **58**, 699 (1986).
13. B. Saager and J. Fischer, *Fluid Phase Equilib.*, **57**, 35 (1990).
14. J. Nagy, D. F. Weaver and V. H. Smith Jr., *J. Phys. Chem.*, **99**, 8058 (1995).
15. H. Stassen, *J. Mol. Struct.: THEOCHEM*, **464**, 107 (1999).
16. S. Murad, K. E. Gubbins and P. Lykos, in *ACS Symp. Ser.*, 62 (1978).
17. W. L. Jorgensen, D. S. Maxwell and J. Tirado-Rives, *J. Am. Chem. Soc.*, **118**, 11225 (1996).
18. A. P. Lyubartsev, A. A. Martsinovski, S. V. Shevkunov and P. N. Vorontsov-Velyaminov, *J. Chem. Phys.*, **96**, 1776 (1992).
19. C. Vega and E. G. Noya, *J. Chem. Phys.*, **127**, 154113 (2007).
20. D. Frenkel and B. Smit, *Understanding Molecular Simulations, 2nd Ed.,* Academic Press, USA (2002).
21. D. A. Kofke, *J. Chem. Phys.*, **98**, 4149 (1993).
22. M. G. Martin and J. I. Siepmann, *J. Phys. Chem. B*, **102**, 2569 (1998).
23. M. Parrinello and A. Rahman, *J. Appl. Phys.*, **52**, 7182 (1981).
24. S. Yashonath and C. N. R. Rao, *Mol. Phys.*, **54**, 245 (1985).
25. M. Kim, J. Chang and S. I. Sandler, *J. Chem Phys.*, **140**, 084110 (2014).
26. D. Frenkel and A. J. C. Ladd, *J. Chem. Phys.*, **81**, 3188 (1984).
27. J. M. Polson, E. Trizac, S. Pronk and D. Frenkel, *J. Chem. Phys.*, **112**, 5339 (2000).
28. N. G. Almarza, *J. Chem. Phys.*, **126**, 211103 (2007).
29. L. A. Báez and P. Clancy, *Mol. Phys.*, **86**, 385 (1995).
30. M. J. Vlot, J. Huinink and J. P. van der Eerden, *J. Chem. Phys.*, **110**, 55 (1999).
31. J. Chang and S. I. Sandler, *J. Chem Phys.*, **125**, 054705 (2006).
32. D. A. McQuarrie, *Statistical Mechanics*, Harper and Row, USA (1976).
33. C. Vega, E. Sanz, J. L. F. Abascal and E. G. Noya, *J. Phys.: Condens. Matter*, **20**, 153101 (2008).
34. G. Perez-Sanchez, D. Gonzalez-Salgado, M. Pineiro and C. Vega, *J. Chem. Phys.*, **138**, 084506 (2013).
35. J. Chang and S. I. Sandler, *J. Chem. Phys.*, **118**, 8390 (2003).
36. J. Chang and S. I. Sandler, *J. Chem Phys.*, **121**, 7474 (2004).
37. J. Chang, A. M. Lenhoff and S. I. Sandler, *J. Phys. Chem. B*, **109**, 19507 (2005).

38. H. C. Andersen, D. Chandler and J. D. Weeks, *J. Chem. Phys.*, **56**, 3812 (1972).
39. A. A. Khare and G. C. Rutledge, *J. Chem. Phys.*, **110**, 3063 (1999).
40. A. A. Khare and G. C. Rutledge, *J. Phys. Chem. B*, **104**, 3639 (2000).
41. G. C. Boulougouris, J. R. Errington, I. G. Economou, A. Z. Panagiotopoulos and D. N. Theodorou, *J. Phys. Chem. B*, **104**, 4958 (2000).
42. J. Chang, *J. Chem. Phys.*, **131**, 074103 (2009).
43. J. Chang, *Korean J. Chem. Eng.*, **28**, 597 (2011).
44. D. N. Bol'shutkin, V. M. Gasan and A. I. Prokhvatilov, *J. Struct. Chem.*, **12**, 670 (1971).
45. J. C. Stryland, J. E. Crawford and M. A. Mastoor, *Can. J. Phys.*, **38**, 1546 (1960).
46. J. D. Grace and G. C. Kennedy, *J. Phys. Chem. Solids*, **28**, 977 (1967).
47. T. Yagi and H. Suzuki, *Proc. Jpn. Acad B*, **66**, 167 (1990).